Notice of Copyright

This Manuscript has been authored by UT-Battelle, LLC, under contract DE-AC05-00OR22725 with the US Department of Energy (DOE). The US government retains and the publisher, by accepting the article for publication, acknowledges that the US government retains a nonexclusive, paid-up, irrevocable, worldwide license to publish or reproduce the published form of this manuscript, or allow others to do so, for US government purposes. DOE will provide public access to these results of federally sponsored research in accordance with the DOE Public Access Plan (hxxp://energy.gov/download/doe-public-access-plant).

Influence of Doping and Thickness on Domain Avalanches in Lead Zirconate Titanate Thin Films

Travis Peters¹, Wanlin Zhu¹, Marti Checa², Liam Collins², Susan Trolier-McKinstry^{1*}

¹ Materials Research Institute, The Pennsylvania State University, University Park, Pennsylvania, 16802, United States

²Center for Nanophase Materials Sciences, Oak Ridge National Laboratory, Oak Ridge, Tennessee 37831, United States

Corresponding Author: Susan Trolier-McKinstry¹, Email: set1@psu.edu Phone: 1+(814) 863-8348

Keywords: Pb(Zr_xTi_{1-x})O₃ (PZT) ceramics, Domain wall motion, Rayleigh Law, Piezoresponse force microscopy

Abstract

In undoped lead zirconate-titanate (PZT) films 1-2 μm thick, domain walls move in clusters with a correlation length of approximately 0.5–2 μm. Band excitation piezoresponse force microscopy (BE-PFM) mapping of the piezoelectric nonlinearity revealed niobium (Nb) doping increases the average concentration or mobility of domain walls *without* changing the cluster area of correlated domain wall motion. In contrast, manganese (Mn) doping reduces the contribution of mobile domain walls to the dielectric and piezoelectric responses without changing the cluster area for correlated motion. In both Nb and Mn doped films, cluster area increases and cluster density drops as the film thickness rises from 250 to 1250 nm. This is evident in spatial maps generated from the analysis of irreversible to reversible ratios of the Rayleigh coefficients.

Introduction

Lead zirconate titanate (PZT) with a composition at the morphotropic phase boundary is widely utilized in sensing, actuating, and transducing applications due to its high piezoelectric coefficients, low dissipation factor, comparatively temperature-stable performance, and facile ceramic processing capability. PZT is modified for specific applications to control the relative amount of domain wall motion at electric fields well below the coercive field [1-4]. Donor doping of PZT ceramics, for example by substituting Nb⁵⁺ and Ta⁵⁺ on the (Zr/Ti)⁴⁺ site, is charge compensated largely by lead-site vacancies in the crystal lattice, along with a smaller population of electrons; donor doping produces "soft PZT". Conversely, acceptor additives such as Mn³⁺ and Fe³⁺ on the (Zr/Ti)⁴⁺ site produce "hard PZT" by generating oxygen vacancies in the lattice and a smaller population of holes.

Accompanying these changes in the defect chemistry are changes in the domain wall contributions to the permittivity, piezoelectric coefficients, and elastic stiffness. In hard PZT, the domain walls are "hard" to move, such that the extrinsic contribution to the macroscopic response is modest. In contrast, the domain contributions to the functional properties in soft PZT are more substantive [5–12].

Despite the widely documented importance of domain wall motion, there are still numerous unknowns about how to quantitatively describe the macroscopic response as a function of local microscopic behavior. For instance, it is now well established that in both single crystal and polycrystalline samples, domain walls move collectively during the switching process, such that motion of one domain wall often triggers an avalanche of correlated motion. These avalanches have been reported to be favored at kinks or junctions of different types of domain walls [13–19]. Correlated switching has also been linked to the existence of a random distribution of defects with widely varying pinning potentials [20]. However, the link between

collective motion and correlative switching of domains to the macroscopic piezoelectric behavior is not well known.

Boser demonstrated that a uniform distribution of restoring forces induces Rayleigh-like responses of the domain walls at fields well below the coercive field [21]. Rayleigh behavior of the dielectric and piezoelectric responses has been widely observed in macroscopic measurements of lead-based films clamped to Si substrates [9-11],[22-30]. Rayleigh behavior in the piezoelectric response even at very local scales is, in and of itself, an indication that domain wall motion must be correlated, such that a Gaussian distribution of restoring forces can be sampled over the correlation volume. Bintachitt et al. experimentally demonstrated collective motion of domain walls in ferroelectric films, as opposed to the motion of noninteracting walls, via nonlinear band excitation piezoresponse force microscopy (BE-PFM) measurements of undoped PZT films. It was found that the correlation length for motion of domain walls was typically $\sim 0.5-2~\mu m$ in films clamped to their underlying substrate, where this dimension was much larger than either the grain size or the domain size [31]. Marincel et al. found that individual microstructural features (e.g. grain boundaries) produce pinning sites that also affect domain wall motion for length scales up to $\sim 800~n m$ [32-34].

Given this background, it is interesting to ask whether donor and acceptor doping of PZT films influences not just the mobility of domain walls, but their correlation length over which clusters of domain walls move cooperatively. That is the goal of this paper.

Experimental Procedure

Sample Fabrication

Two sets of samples were created to investigate the influence of thickness and dopants on the domain clusters in PZT films on silicon substrates: (1) 2 mol% Nb doped Pb(Zr_{0.52}Ti_{0.48})O₃ (PNZT) films with thicknesses from 288 nm to 1210 nm; (2) 2 mol% Mn doped Pb(Zr_{0.52}Ti_{0.48})O₃ (PMZT) films from 222 nm to 1265 nm. Table 1 shows each PNZT and PMZT film thickness. The commercial chemical solution (PZT-E1, Mitsubishi Materials Corporation, Tokyo, Japan) used for the seed layer, bulk layer and top layer are described in detail elsewhere [35]. These average compositions are at the morphotropic phase boundary for PZT. It is noted, though, that the films were prepared by chemical solution deposition, which induces Zr/Ti gradients associated with each crystallization step, as reported previously [36].

500 µm diameter, 100 nm thick platinum top electrodes were deposited by DC-sputtering and patterned by a standard lift-off process for electrical characterization.

Table 1: PNZT and PMZT films.

Film	Thickness (nm)	Film	Thickness (nm)
2mol% Nb-PZT	288	2mol% Mn-PZT	222
	528		498
	775		773
	1022		1085
	1210		1265

Piezoresponse Force Microscopy

The AFM used in this study was a commercial Cypher AFM (Asylum Research, Santa Barbara, CA). All PFM measurements were taken with Pt-coated cantilevers (PPP-EFM) with a nominal spring constant of \sim 3 N/m and resonance frequency of \sim 75 kHz. BE-PFM was performed using external data acquisition electronics based on a NI-6115 fast DAQ card controlled by custom-built Labview software. A voltage signal around the cantilever contact resonance frequency, which combined chirp and sync waveforms, was applied to the AFM probe and electrode capacitor. This enabled quantitative *local* measurements of piezoelectric nonlinearity while having a defined uniform electric field as previously described [31]. Prior to PFM measurements, each capacitor was poled with a probe station at 150°C for 15 minutes at 3x the average coercive voltage (V_o). Table S1 (Supplemental Materials) shows the coercive field and poling voltage for each PZT film. PFM measurements were initiated no sooner than 60 minutes after the DC bias was removed to reduce artefacts from aging. The PFM experimental data was stored in h5 files and post-processed using the python pycroscopy package [37].

Nonlinear BE-PFM experiments involved linearly increasing the bias voltage excitation amplitude from 0 to $\sim 1/2~V_c$, where V_c is the coercive voltage of the sample, in the frequency range of 325-360 kHz. The conductive probe and top electrode were driven with the same excitation function while the bottom electrode was grounded, which helped to minimize electrostatic contributions. To minimize potential measurement artifacts due to nonlinear cantilever dynamics, resonance peak asymmetry was analyzed by chirping up and down in frequency space as described previously [38]. The phase of the chirp wave was tuned closer to a sync, so that both chirp sweeps contained symmetric and overlapping resonance peaks. Spectroscopic maps were collected on a two-dimensional grid on the electrode surface. The resultant

multidimensional dataset was a function of frequency, amplitude, excitation voltage, and two spatial coordinates.

Data Analysis

A simple harmonic oscillator equation (SHO) was used to fit the cantilever response as a function of frequency for each voltage step and position, obtaining the corresponding amplitude at resonance (A_{max}) , resonant frequency (ω_o) , and mechanical quality factor (Q). The nonlinear function of A_{max} was described by a second-order polynomial $A_{max} = A_0 + A_1 * E_{AC} + A_2 * E_{AC}^2$; differentiation with respect to the electric field yielded the Rayleigh law [31]. The ratio of the Rayleigh coefficients associated with irreversible (α_{d33}) and reversible $(d_{33,initial})$ contributions is given by $2A_2/A_1$, where A_2 is the quadratic coefficient, A_1 is the linear coefficient, and A_0 is the intercept of the second-order polynomial. As previously noted, A_0 was assigned to 0 * [31]. Excitation amplitudes below the detection range of BE-PFM were excluded from the quadratic fit with a threshold being an SHO coefficient of determination (R^2) greater than 0.5.

K-means clustering [39] was performed on each $\alpha_{d33}/d_{33,initial}$ spatial map to group datapoints with similar response into three clusters: low, medium, and high response. The k-means clustered spatial map was binarized so that each pixel containing a Rayleigh ratio in the highest bin received a value of 1 and all other pixels were 0. A median filter was applied to the binary image, and a python label "blobbing" function [40] determined the number of clusters and the area of each cluster (in μ m²). An identical analysis was repeated for all ten PZT film nonlinear BE-PFM measurements.

Results & Discussion

All PZT films exhibited a <100> preferred orientation as confirmed by Bragg-Brentano x-ray diffraction (XRD) patterns (see Supplemental Materials, Figure S1). Figure 1 shows the XRD pattern of Mn-doped and Nb-doped PZT films, ~500 and ~1000 nm thick, around the 100 PZT peak. The Shannon-Prewitt effective ionic radii of Nb⁵⁺ and Mn³⁺ in octahedral coordination are 64 pm and 58 pm, respectively [41]. The 100 XRD peak in both Nb-doped PZT films shifted to a lower 2θ value, corresponding to a larger out of plane unit cell lattice spacing. No thickness dependence on lattice parameter was observed for a given dopant.

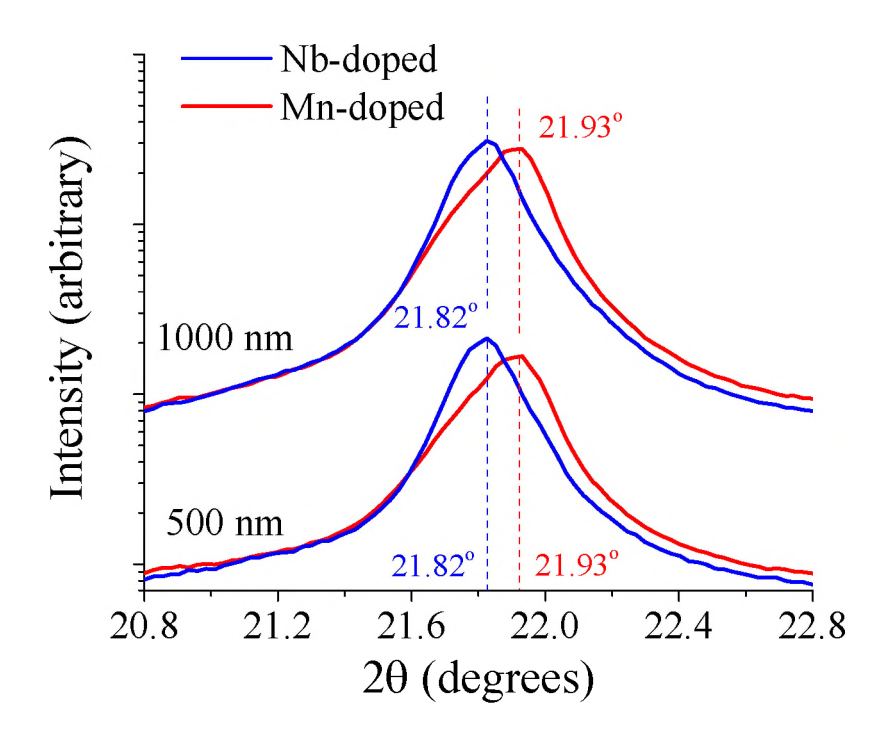


Figure 1: Bragg-Brentano x-ray diffraction analysis of 500 nm and 1000 nm thick PZT films doped with Mn and Nb near the 100 PZT peak.

Figure 2a illustrates the experimental setup for nonlinear BE-PFM measurements. All measurements were performed on capacitors, such that the probe acted as a strain sensor and the electric field distribution across the film was homogeneous and quantifiable. The piezoresponse at each point was captured across the frequency band centered on the resonant frequency of the cantilever (\sim 345 kHz) for both chirp directions, as shown in Figure 2b. The resultant SHO maximum amplitude (A_{max}) is plotted as a function of applied AC electric field in Figure 2c for a single pixel, which was fitted with the quadratic polynomial $A_{max}=A_1*E_{AC}+A_2*E_{AC}^2$ represented as the blue curve. The black data point in Figure 2c represent the excitation amplitudes below the detection range of BE-PFM; such points were excluded from the quadratic fit.

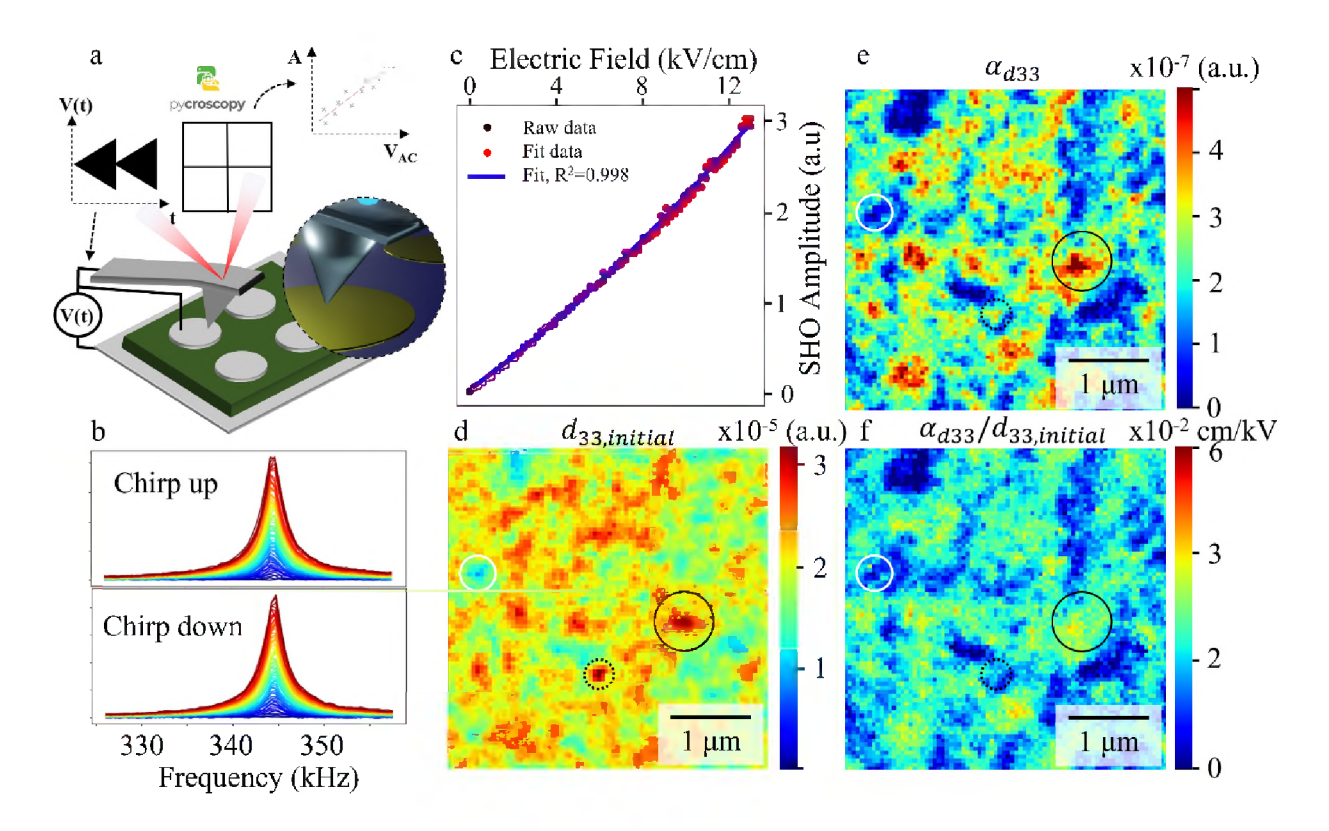


Figure 2: BE-PFM results of the Mn-doped 500 nm thick PZT film. (a) A schematic of the experimental setup. (b) The phase of the chirp wave tuned closer to a sync value, producing overlapping resonance peaks for both frequency chirp directions. (c) An example of the resonance amplitude quadratic fit for a single pixel, with the black data points excluded from the fit. (d) A map of A_2 (proportional to $d_{33,initial}$) (e) Map of the A_3 (proportional to a_{d33}) (f) The $a_{d33}/d_{33,initial}$ ratio map.

The piezoelectric amplitude is directly proportional to sample displacement h, $A_{max} = \beta h$, where β is cantilever sensitivity [31]. The Rayleigh law is extracted by the differentiation of A_{max} : $\beta d_{33,f} = \beta d_{33,initial} + 2\beta \alpha_{d33} E_{AC}$, where $d_{33,f}$ is the piezoelectric coefficient, $A_1 \propto d_{33,initial}$ and $2A_2 \propto \alpha_{d33}$. Evidence of domain wall clustering is displayed in Figure 2d, which shows the spatial map of Rayleigh coefficient $d_{33,initial}$. Similarly, Figure 2e shows clusters with higher α_{d33} , or irreversible domain wall contributions, compared to the lower α_{d33} matrix. The $\alpha_{d33}/d_{33,initial}$ map displayed in Figure 2f also shows clustering of the extrinsic response.

The $d_{33,initial}$ map illustrates the presence of large-scale features, which range from hundreds of nanometers to 2 micrometers. The α_{d33} map also illustrates micron-sized clusters. It is noted that the $d_{33,initial}$ and α_{d33} cluster maps are largely decoupled from one another. This is visualized in Figure 2 (d-f), where the solid black circles show regions of high $d_{33,initial}$ and high α_{d33} coefficients while the dotted black circles show regions of high $d_{33,initial}$ but low α_{d33} coefficients. The white circles highlight regions where both $d_{33,initial}$ and α_{d33} responses are low.

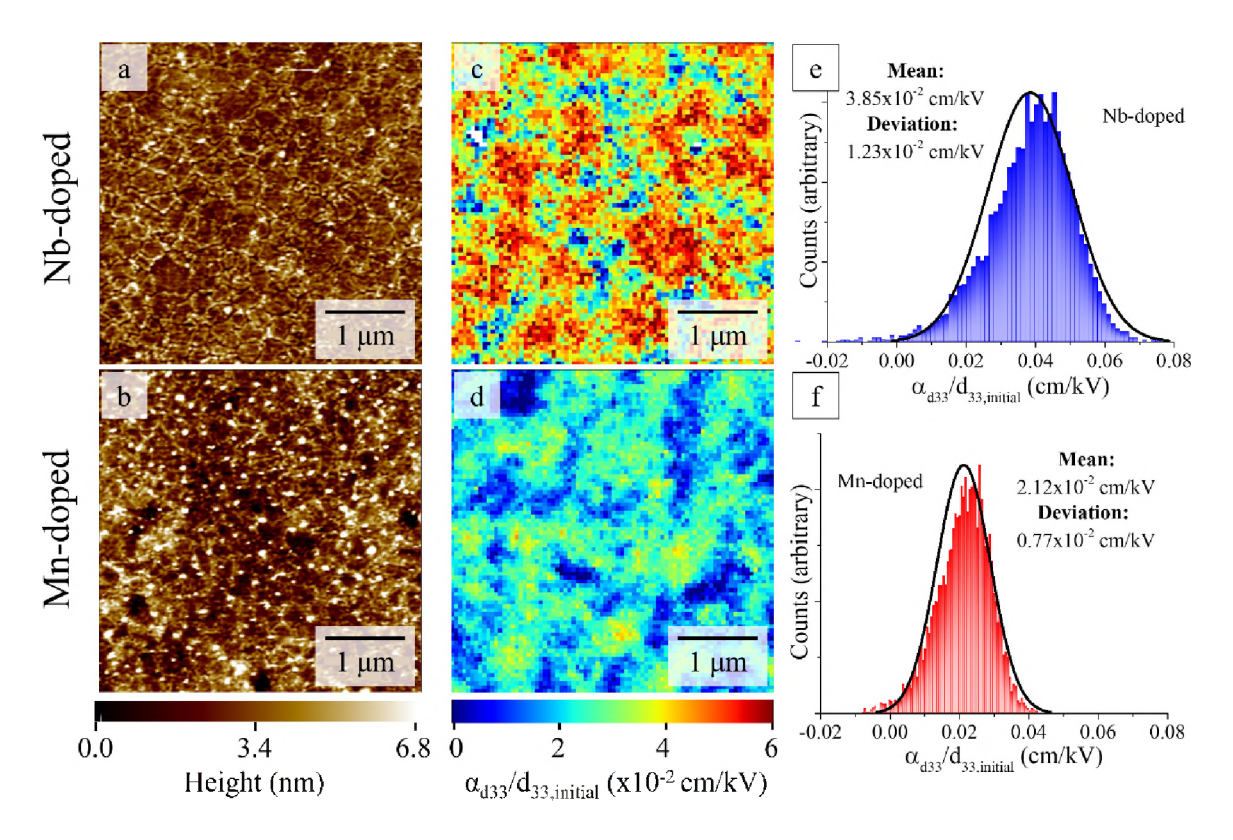


Figure 3: Contact atomic force microscopy topography maps of 500 nm thick PZT films doped with Nb (a) and Mn (b). Nonlinear Rayleigh ratio maps for 500 nm thick PZT film doped with Nb (c) and Mn (d). Histograms of nonlinear Rayleigh ratio maps (c/d) for Nb (e) and Mn (f) doped PZT films, with black lines as Gaussian fits.

Figure 3 (a,b) show the topography of the 500 nm thick Nb and Mn doped PZT film surfaces, respectively, measured with contact mode AFM. The average in-plane grain area for the 500 nm thick Nb-doped film was $33 \times 10^{-3} \pm 7 \times 10^{-3} \, \mu m^2$ and $20 \times 10^{-3} \pm 2 \times 10^{-3} \, \mu m^2$ for the Mn-doped film. Grain area analysis was performed with scanning electron microscopy and the line intercept method, which is shown in Figure S2 of Supplemental Materials. The average surface roughness for both films does not exceed 1.3 nm. Additionally, it should be noted that there were small differences between the electrical conductivity of the donor and acceptor doped films; as is typical in PZT, the majority of the doping was ionically compensated, rather than electronically compensated [42-44]. The conductivity between films of donor and acceptor doping was not expected to differ significantly.

A comparison of spatially resolved nonlinear Rayleigh ratio maps from BE-PFM are presented in Figure 3 (c,d) for Nb and Mn-doped films, respectively. High response clusters with areas 0.1 to 1 μ m², much larger than the average grain area in each film, can be observed. Histograms of the nonlinear Rayleigh ratios for Nb and Mn doped films are shown in Figure 3 (e,f), respectively, with average $\alpha_{d33}/d_{33,initial}$ ratios

of 38.5×10^{-3} cm/kV and 21.2×10^{-3} cm/kV, respectively. The black lines in Figure 3 (e,f) are Gaussian fits to the Rayleigh ratio histograms which do not fully fit the spatial distribution of $\alpha_{d33}/d_{33,initial}$ ratios. There is a slight skew of the histogram data to a smaller ratio in both films. The higher nonlinearities in the Nb doped PZT film are related to reduced domain wall pinning, as is typical in bulk donor doped PZT ceramics [11].

Importantly, the cluster areas are similar between the two films even though the $\alpha_{d33}/d_{33,initial}$ ratio is very different. The $\alpha_{d33}/d_{33,initial}$ maps for Nb and Mn doped PZT films displayed in Figure 3 (c,d) were processed to calculate individual high response cluster areas. The image processing was performed with the scikit learn [39] and scikit image [40] analysis tools in Python, and the individual steps are shown in Figure S3 in Supplemental Materials.

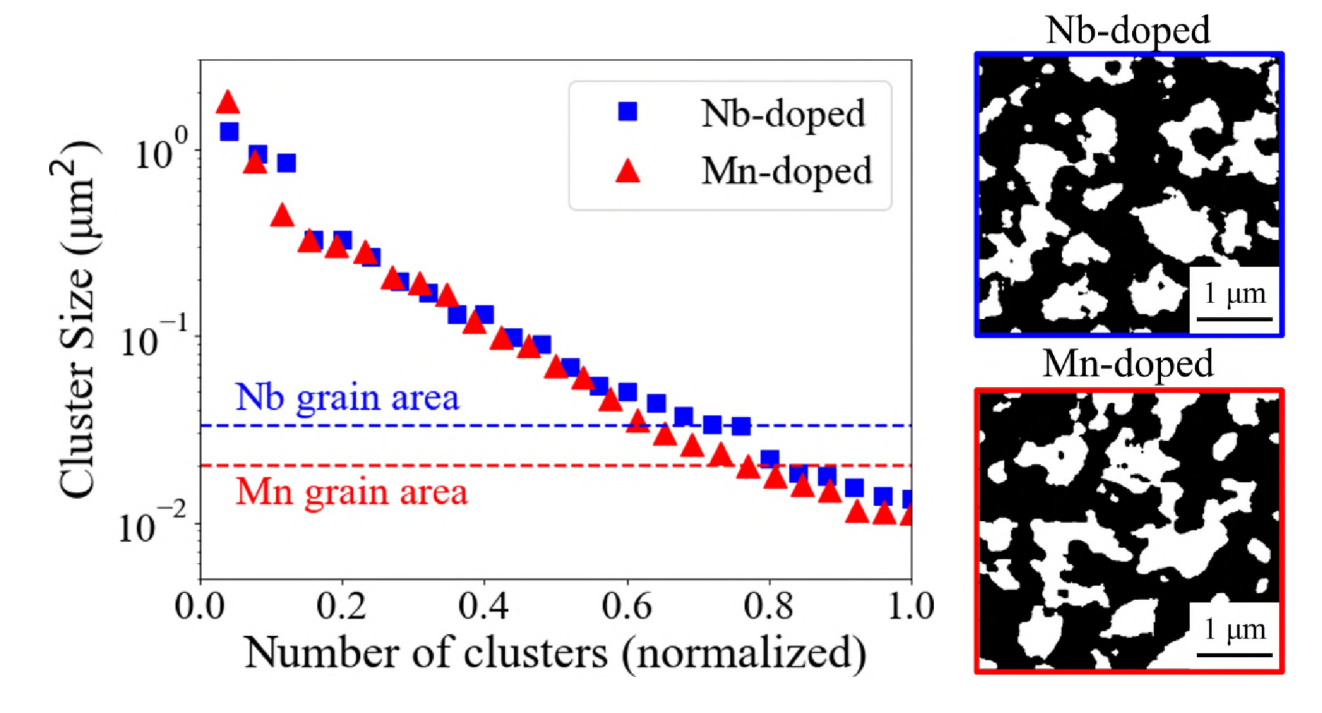


Figure 4: High mobility cluster areas in Nb-doped (blue) and Mn-doped (red) PZT films 500 nm thick. The white regions (right-side cluster maps) are regions which had high $\alpha_{d33}/d_{33,initial}$ responses.

A closer examination of the individual cluster areas for 500 nm thick Nb-doped (blue) and Mn-doped (red) PZT films is given in Figure 4. The left-side plot displays the distribution of cluster areas, with the horizontal dashed lines representing the average grain areas for the two films. The right-side images are the binary spectroscopic maps of high response Rayleigh clusters in white; both medium and low response regions are shown in black. Of the twenty-five clusters larger than 0.01 µm², 76% are bigger than the average grain area in Nb-doped PZT and 77% are bigger than the grain area in Mn-doped PZT. More than

75% of the high Rayleigh response clusters in each film are larger than the average grain area, demonstrating domain avalanche characteristics across grain boundaries.

Another recent report demonstrates the triggering of coupled motion of ferroelastic twin boundaries in SrTiO₃ by weak mechanical vibrations ^[45]. In SrTiO₃, this occurs dynamically at temperatures below 100K. Here, in PZT, the long range coupling for small signal excitations is shown to occur at room temperature. Furthermore, clusters in the range of 0.01 µm² to 2 µm² are independent of dopant type, demonstrated by the overlapping trend of cluster area versus the normalized cluster number. Thus, the correlation length for the motion of domain walls is comparable for both donor and acceptor-doped films. This suggests that the size of domain avalanches is unaffected by lead or oxygen vacancies at the 2% dopant levels in 500 nm thick PZT films. The combination of the data in Figures 3 and 4 suggests that extrinsic contributions are suppressed everywhere (e.g. at very small volumes) in the Mn-doped films, and enhanced at very small volumes in the Nb-doped films. That is, point defects do not govern the spatial extent of correlated domain walls, just their local mobility.

An identical analysis of the spectroscopic $\alpha_{d33}/d_{33,initial}$ ratios for each Nb doped and Mn doped PZT film between 250 nm and 1250 nm thick enabled evaluation of cluster characteristics in films of varying thickness. The results are shown in Figure 5, which displays the binary Rayleigh response clusters (with white regions as the high response clusters) for each film thickness. It was found that as PZT film thickness increased, the total number of clusters greater than 0.01 μ m² in size within a 4x4 μ m² scan size decreased. This trend is also shown in the right-most plot in Figure 5. There is no clear difference in the number of clusters between the films with different dopant types, as the Nb-doped and Mn-doped results largely superimpose in the range of film thicknesses investigated.

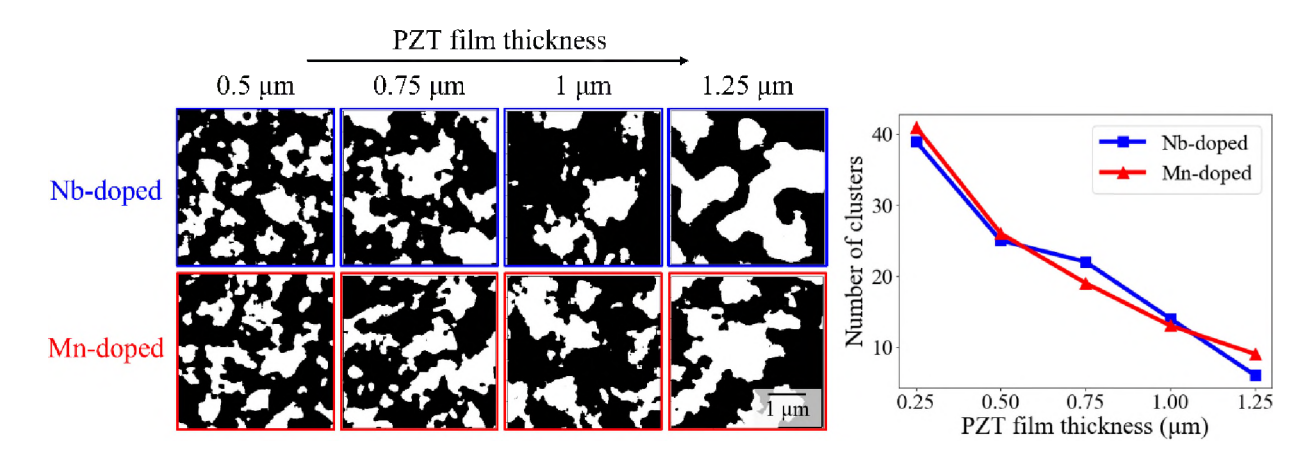


Figure 5: Binarized cluster maps showing regions of high nonlinearity (white) in a matrix of medium and low nonlinearity (black) for 4x4 μm² scan sizes. The right-most figure shows the number of clusters as a function of film thickness for Nb-doped (blue) and Mn-doped (red) PZT films.

An evaluation of the cluster areas in each PZT film is shown in Figure 6 (a) and (b) for Nb-doped and Mn-doped films, respectively. The bar charts represent trends between individual cluster area and PZT film thickness. First, in both Nb and Mn doped films, the thinner films contain more clusters in a $4x4~\mu m^2$ area, visualized by the long tails extending to $0.01~\mu m^2$ cluster area for the 250 nm thick film (red). The thicker films (e.g. 1250 nm film in grey) have relatively few clusters, each one larger than the majority of clusters in the thinner films. Second, the total cluster area and the number of clusters for each film is independent of dopant type but is dependent on the film thickness. The high response clusters represent 32% and 33% of the $16~\mu m^2$ scan region for the Nb-doped and Mn-doped 500 nm thick films, respectively. However, the 250 nm Mn-doped film contains 8% high response (clustered) regions compared to 42% high response regions for the Mn-doped 1250 nm (Figure 6b).

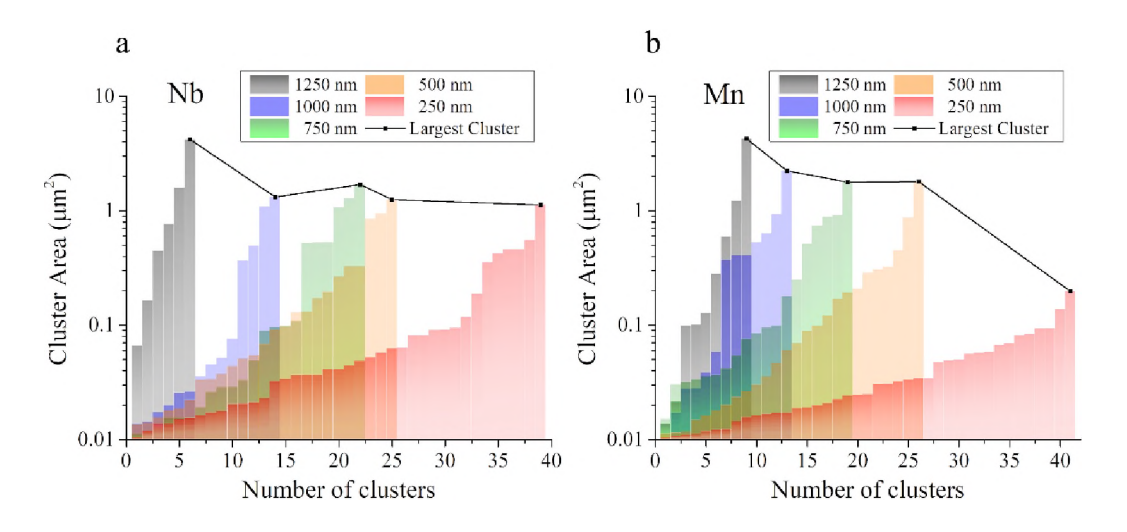


Figure 6: Bar charts for Nb-doped (a) and Mn-doped (b) PZT films from 250 nm to 1250 nm thick, showing the cluster area for each identified cluster larger than 0.01 μm².

Finally, the black lines in Figure 6 indicate that as film thickness increases for films with both dopant types, the largest cluster observed in the analysis increases. Bassiri-Gharb et al. [9] and Denis et al. [46] reported that for PZT films near ~1 µm thick, domain mobility increased in films of increasing thickness because, either, the potential energy profile for moving domain walls contains increasingly shallow wells, the concentration of pinning sites due to substrate clamping is lower, or the mobility of existing domain walls increases [9]. In this study, as film thickness increases from 250 nm to 1250 nm, the avalanche characteristics indicate more collective irreversible motion of domain walls, possibly because with increased thickness, there is a higher probability of a region which couples well to adjacent regions laterally.

Conclusions

This work describes how dopants and film thickness affect clustering of irreversible domain wall motion in Nb- and Mn-doped PZT films that are 250 nm to 1250 nm thick. Nonlinear band excitation piezoresponse force microscopy measurements enabled local spectroscopic mapping of irreversible to reversible Rayeigh ratios in $4x4~\mu m^2$ regions. It was found that domain clustering exists in both Nb- and Mn-doped PZT films in this thickness regime, with cluster areas as small as PZT grains ($\sim 20x10^{-3}~\mu m^2$) and as large as $4.2~\mu m^2$ in the ~ 1250 nm thick films with each dopant type. The individual cluster areas increased with increasing film thickness but did not depend on the dopant or crystalline vacancy defect type. As film thickness increased, cluster density decreased and the percent of high response regions in a $4x4~\mu m^2$ scan area increased, indicating more collective irreversible motion of domain walls.

Supplementary Material

Supplementary materials include the poling conditions for all films, X-ray diffraction patterns and scanning electron micrograph images of the 500 nm thick films for both dopants, and an example image analysis separating high response clusters.

Acknowledgements

Support for this work was provided in part by SCGSR Fellowship and corresponding CNMS user proposal CNMS2022-B-999 (T.P. and S.T.-M.). Other funding was provided by the National Science Foundation [grant number NSF EEC-1160483] and the Flaschen Professorship. PFM research was supported by the Center for Nanophase Materials Sciences (CNMS), which is a US Department of Energy, Office of Science User Facility at Oak Ridge National Laboratory.

References

- [1] B. Jaffe, W. R. Cook, H. Jaffe, *Piezoelectric ceramics* (Eds.: Roberts, J. P.; Popper, P.), London, 1971.
- [2] D. Berlincourt, J. Acoust. Soc. Am. 1992, 91, 3034.
- [3] D. Berlincourt, In *Ultrasonic Transducer Materials*, Springer, Boston, MA, 1971, pp. 63–124.
- [4] S. Trolier-McKinstry, S. Zhang, A. J. Bell, X. Tan, Annu. Rev. Mater. Res. 2018, 48, 191.
- [5] S. Li, W. Cao, L. E. Cross, J. Appl. Phys. 1991, 69, 7219.
- [6] D. Damjanovic, M. Demartin, J. Phys. Condens. Matter 1997, 9, 4943.
- [7] D. A. Hall, Ferroelectrics 1999, 223, 319.
- [8] D. A. Hall, J. Mater. Sci. 2001, 36, 4575.
- [9] N. Bassiri-Gharb, I. Fujii, E. Hong, S. Trolier-McKinstry, D. V. Taylor, D. Damjanovic, *J. Electroceramics* **2007**, *19*, 47.

- [10] W. Zhu, I. Fujii, W. Ren, S. Trolier-McKinstry, J. Appl. Phys. **2011**, 109, 0.
- [11] W. Zhu, I. Fujii, W. Ren, S. Trolier-McKinstry, J. Am. Ceram. Soc. 2012, 95, 2906.
- [12] T. Rojac, D. Damjanovic, *Jpn. J. Appl. Phys.* **2017**, *56*, 1.
- [13] W. Cao, C. A. Randall, J. Phys. Chem. Solids 1996, 57, 1499.
- [14] C. A. Randall, N. Kim, J. P. Kucera, W. Cao, T. R. Shrout, J. Am. Ceram. Soc. 1998, 81, 677.
- [15] J. Y. Li, R. C. Rogan, E. Üstündag, K. Bhattacharya, *Nat. Mater.* **2005**, *4*, 776.
- [16] B. Casals, G. F. Nataf, D. Pesquera, E. K. H. Salje, *APL Mater.* **2020**, 8.
- [17] B. Casals, G. F. Nataf, E. K. H. Salje, Nat. Commun. 2021, 12, 1.
- [18] J. Schultheiß, L. Liu, H. Kungl, M. Weber, L. Kodumudi Venkataraman, S. Checchia, D. Damjanovic, J. E. Daniels, J. Koruza, *Acta Mater.* **2018**, *157*, 355.
- [19] J. Schultheiß, S. Checchia, H. Uršič, T. Frömling, J. E. Daniels, B. Malič, T. Rojac, J. Koruza, *J. Eur. Ceram. Soc.* **2020**, *40*, 3965.
- [20] E. K. H. Salje, D. Xue, X. Ding, K. A. Dahmen, J. F. Scott, *Phys. Rev. Mater.* **2019**, *3*, 14415.
- [21] O. Boser, J. Appl. Phys. 1987, 62, 1344.
- [22] L. M. Denis, G. Esteves, J. Walker, J. L. Jones, S. Trolier-McKinstry, Acta Mater. 2018, 151, 243.
- [23] L. M. Denis-Rotella, G. Esteves, J. Walker, H. Zhou, J. L. Jones, S. Trolier-McKinstry, *IEEE Trans. Ultrason. Ferroelectr. Freq. Control* **2021**, *68*, 259.
- [24] N. B. Gharb, S. Trolier-McKinstry, *J. Appl. Phys.* **2005**, *97*.
- [25] S. Trolier-McKinstry, N. B. Gharb, D. Damjanovic, Appl. Phys. Lett. 2006, 88.
- [26] N. B. Gharb, S. Trolier-McKinstry, D. Damjanovic, J. Appl. Phys. 2006, 100.
- [27] W. Zhu, W. Ren, H. Xin, P. Shi, X. Wu, J. Adv. Dielectr. 2013, 03, 1350011.
- [28] F. Griggio, S. Jesse, W. Qu, A. Kumar, O. Ovchinnikov, D. S. Tinberg, S. V. Kalinin, S. Trolier-McKinstry, *J. Appl. Phys.* **2011**, *110*, 0.
- [29] F. Griggio, S. Jesse, A. Kumar, O. Ovchinnikov, H. Kim, T. N. Jackson, D. Damjanovic, S. V. Kalinin, S. Trolier-McKinstry, *Phys. Rev. Lett.* **2012**, *108*, 1.
- [30] R. Keech, C. Morandi, M. Wallace, G. Esteves, L. Denis, J. Guerrier, R. L. Johnson-Wilke, C. M. Fancher, J. L. Jones, S. Trolier-McKinstry, *J. Am. Ceram. Soc.* **2017**, *100*, 3961.
- [31] P. Bintachitt, S. Jesse, D. Damjanovic, Y. Han, I. M. Reaney, S. Trolier-McKinstry, S. V. Kalinin, *Proc. Natl. Acad. Sci. U. S. A.* **2010**, *107*, 7219.
- [32] D. M. Marincel, H. Zhang, A. Kumar, S. Jesse, S. V. Kalinin, W. M. Rainforth, I. M. Reaney, C. A. Randall, S. Trolier-McKinstry, *Adv. Funct. Mater.* **2014**, *24*, 1409.
- [33] D. M. Marincel, H. Zhang, S. Jesse, A. Belianinov, M. B. Okatan, S. V. Kalinin, W. M. Rainforth, I. M. Reaney, C. A. Randall, S. Trolier-McKinstry, *J. Am. Ceram. Soc.* **2015**, *98*, 1848.
- [34] D. M. Marincel, H. R. Zhang, J. Britson, A. Belianinov, S. Jesse, S. V. Kalinin, L. Q. Chen, W. M. Rainforth, I. M. Reaney, C. A. Randall, S. Trolier-McKinstry, *Phys. Rev. B Condens. Matter Mater. Phys.* **2015**, *91*.

- [35] W. Zhu, B. Akkopru-Akgun, J. I. Yang, C. Fragkiadakis, K. Wang, S. W. Ko, P. Mardilovich, S. Trolier-McKinstry, *Acta Mater.* **2021**, *219*, 117251.
- [36] F. Calame and P. Muralt, Applied Physics Letters, 2007, 90, 062907.
- [37] S. Somnath, C. R. Smith, N. Laanait, R. K. Vasudevan, S. Jesse, *Microsc. Microanal.* 2019, 25, 220.
- [38] F. Griggio, S. Jesse, A. Kumar, D. M. Marincel, D. S. Tinberg, S. V. Kalinin, S. Trolier-McKinstry, *Appl. Phys. Lett.* **2011**, *98*, 98.
- [39] F. Pedregosa, G. Varoquaux, A. Gramfort, V. Michel, B. Thirion, O. Grisel, M. Blondel, P. Prettenhofer, R. Weiss, V. Dubourg, J. Vanderplas, *JMLR* **2011**, *12*, 2825.
- [40] S. Van der Walt, J. L. Schonberger, J. Nunez-Iglesias, F. Boulogne, J. D. Warner, N. Yager, E. Gouillart, T. Yu, *PeerJ* **2014**, *2*, e453.
- [41] R. D. Shannon, Acta Crystallogr. Sect. A 1976, 32, 751.
- [42] D. Koh, S. W. Ko, J. I. Yang, B. Akkopru-Akgun, S. Trolier-McKinstry, J. Appl. Phys. 2022, 132.
- [43] B. Akkopru-Akgun, D. M. Marincel, K. Tsuji, T. J. M. Bayer, C. A. Randall, M. T. Lanagan, S. Trolier-McKinstry, *J. Am. Ceram. Soc.* **2021**, *104*, 5270.
- [44] N. J. Donnelly, C. A. Randall, J. Appl. Phys. 2011, 109.
- [45] S. Kustov, I. Liubimova, and E. K. H. Salje, Phys. Rev. Lett, **2020**, *124*, 016801.
- [46] L. M. Denis, G. Esteves, J. Walker, J. L. Jones, S. Trolier-McKinstry, Acta Mater. 2018, 151, 243.